SCIENTIFIC REPORTS

OPEN

Unusual dimensionality effects and surface charge density in 2D Mg(OH)$_2$

Aslihan Suslu[1,*], Kedi Wu[1,*], Hasan Sahin[2,*], Bin Chen[1], Sijie Yang[1], Hui Cai[1], Toshihiro Aoki[1,3], Seyda Horzum[2], Jun Kang[2], Francois M. Peeters[2] & Sefaattin Tongay[1]

We present two-dimensional Mg(OH)$_2$ sheets and their vertical heterojunctions with CVD-MoS$_2$ for the first time as flexible 2D insulators with anomalous lattice vibration and chemical and physical properties. New hydrothermal crystal growth technique enabled isolation of environmentally stable monolayer Mg(OH)$_2$ sheets. Raman spectroscopy and vibrational calculations reveal that the lattice vibrations of Mg(OH)$_2$ have fundamentally different signature peaks and dimensionality effects compared to other 2D material systems known to date. Sub-wavelength electron energy-loss spectroscopy measurements and theoretical calculations show that Mg(OH)$_2$ is a 6 eV direct-gap insulator in 2D, and its optical band gap displays strong band renormalization effects from monolayer to bulk, marking the first experimental confirmation of confinement effects in 2D insulators. Interestingly, 2D-Mg(OH)$_2$ sheets possess rather strong surface polarization (charge) effects which is in contrast to electrically neutral h-BN materials. Using 2D-Mg(OH)$_2$ sheets together with CVD-MoS$_2$ in the vertical stacking shows that a strong change transfer occurs from n-doped CVD-MoS$_2$ sheets to Mg(OH)$_2$, naturally depleting the semiconductor, pushing towards intrinsic doping limit and enhancing overall optical performance of 2D semiconductors. Results not only establish unusual confinement effects in 2D-Mg(OH)$_2$, but also offer novel 2D-insulating material with unique physical, vibrational, and chemical properties for potential applications in flexible optoelectronics.

Layered crystals at the quantum confinement (2D) limit are emerging as an important class of materials for information and energy conversion technologies[1,2]. Especially after demonstration and synthesis of 2D materials with finite band gaps, such as h-BN and members of the semiconducting transition metal dichalcogenides (sTMDs) family[3–5], a large number of proof-of-concept devices has been realized[1,6]. In particular, sTMDs have shown great potential in optoelectronics applications owing to their unusual properties in the quantum confinement limit[7–11]. However, unlike the vast number of existing conventional materials where their gap values almost continuously cover from near infrared (NIR) to deep UV, the full potential of these 2D materials is mostly limited by their energy gaps, band alignment properties, and, with respect to 3D materials, offers a relatively small number of materials to choose from.

Here, we experimentally and theoretically report on the physical, chemical, and lattice vibrations of 2D Mg(OH)$_2$, a member of alkaline metal hydroxides (AMHs), for the first time. By modified Mg(OH)$_2$ hydrothermal synthesis technique, we successfully isolated 2D Mg(OH)$_2$ from highly crystalline, large domain size, and layered Mg(OH)$_2$ crystals. Raman spectroscopy measurements on Mg(OH)$_2$ show that the lattice vibration characteristics and their dimensionality dependence are in stark contrast to other 2D materials known to date. Instead of first-order Raman peaks, the lattice vibration characteristics of 2D Mg(OH)$_2$ are mostly dominated by two hydroxyl (–OH) group in-phase and out-of-phase vibration modes ($A_{1g}^{OH(1,2)}$) which appear at 3642 and 3651 cm^{-1}. A_{1g}^{OH} peak position and shape strongly depend on the interaction between –OH groups in the adjacent layers and, in 2D, Raman spectrum reduces to out-of-plane mode. Nanoscale sub-wavelength electron energy-loss spectroscopy (nano-EELS) measurements correlate with the electronic structure to the dimensionality of the Mg(OH)$_2$, showing the band renormalization effects on 2D insulating materials. Owing to the strong

[1]School for Engineering of Matter, Transport and Energy, Arizona State University, Tempe, AZ, 85287, USA. [2]Department of Physics, University of Antwerp, Campus Groenenborger, Groenenborgerlaan 171, 2020, Antwerp, Belgium. [3]LeRoy Eyring Center for Solid State Science, Arizona State University, Tempe, AZ 85287, USA. *These authors contributed equally to this work. Correspondence and requests for materials should be addressed to S.T. (email: Sefaattin.Tongay@asu.edu)
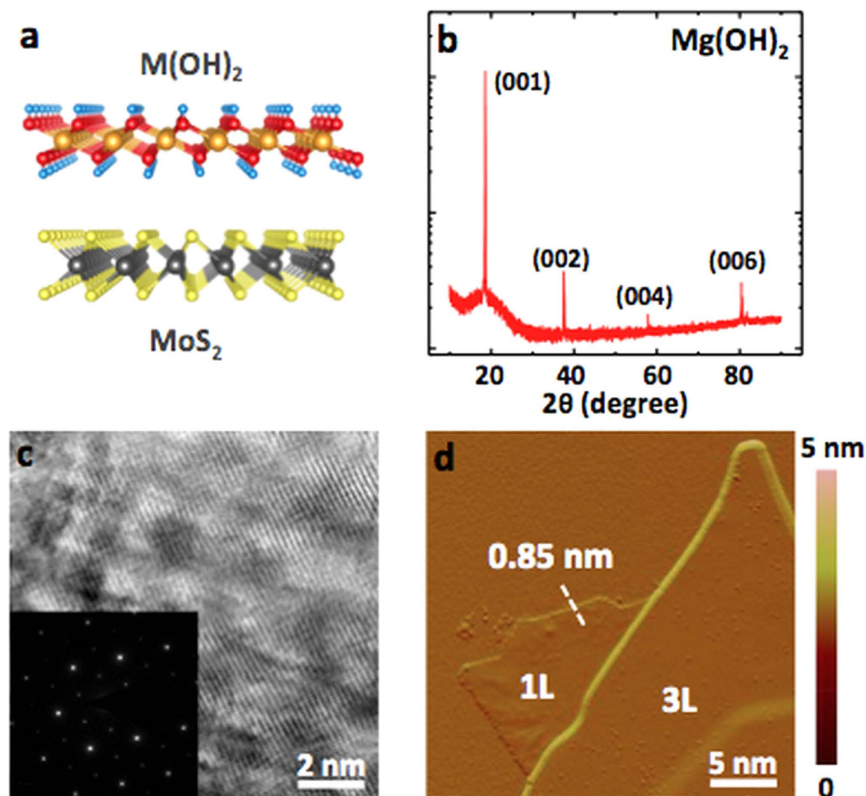
Figure 1. AMHs crystal structure and characterization (**a**) Structural comparison between MoS_2, a member of TMDCs and $Mg(OH)_2$ from AMHs family. (**b**) XRD pattern taken directly from $Mg(OH)_2$ crystals. (**c**) Transmission electron microscopy image and SAED pattern taken from synthesized crystals displaying the crystallinity and 1T lattice structure. (**d**) Atomic force microscopy images taken from monolayer and few-layer $Mg(OH)_2$.

polarization at the AMHs surface (induced by the hydroxyl group), vertical stacking of $Mg(OH)_2/MoS_2$ enables tuning the MoS_2 properties as evidenced by much enhanced photoluminescence (PL) emission and shifted PL peak position. Overall results expand the library of 2D materials towards insulating counter-parts, offering a new class of 2D insulating materials with unique physical, chemical, and vibrational properties.

Structure, crystal growth, and 2D Mg(OH)$_2$ sheets

Alkaline earth metal hydroxides are a family of layered crystals with the general formula $M(OH)_2$, where M is alkaline metal from group IIA elements such as Ca and Mg[12,13]. Similar to transition metal dichalcogenides (TMDs), alkaline hydroxides belong to the P3m1 (Hermann-Mauguin notation) space group, except the unit cell consists of one alkaline metal group element (Ca, Mg) symmetrically bonded to two hydroxide groups in the T-phase as opposed to observed H-phase in group VI TMDs (e.g. MoS_2, WS_2) as shown in Fig. 1a.

Previously, AMHs crystals were synthesized by hydrothermal growth routes in small autoclave reactors in nanoparticle or micro-sized crystallite form, but small, single-domain size and poor control over their growth dynamics prevented achieving 2D- and few-layer (quasi-2D) AMHs sheets. To synthesize larger size and highly crystalline $Mg(OH)_2$, alkaline metal nitrates, $Mg(NO_3)_2$ were first heated to 125–140 °C for six hours in a stainless steel autoclave (250 mL), immediately reacted with ammonia (NH_3) for a week at 5–10 MPa[13–15], and slowly cooled to room temperature at controlled rates after six days. Typical synthesis process yields ~1 mm up to cm-sized crystals dispersed in the bi-product solution. Materials were finally filtered using micropore filters and washed by DI water. Sharp (001) peaks located at multiples of 18.55° (Fig. 1b), associated with the Bragg reflections from layers stacked in the c-axis direction, confirm the crystallinity of the materials. The lattice spacing is estimated around ~4.86 A°, which is close to the values calculated by our DFT calculations (~4.95 A°).

Transmission electron microscopy (TEM) image and selected area electron diffraction (SAED) pattern also confirm high crystallinity of the synthesized materials as shown in Fig. 1c for $Mg(OH)_2$ where the SAED pattern displays a hexagonal pattern expected from tetragonal distorted AMHs monolayers with three-fold symmetry. Here, we note that the monolayers quickly decomposed under an 80 keV e-beam, possibly due to the low melting point of $Mg(OH)_2$, preventing us from capturing high resolution TEM images.

We isolated monolayer $Mg(OH)_2$ from synthesized bulk crystals by mechanical exfoliation onto piranha cleaned 285 nm thermal SiO_2/Si substrates for improved contrast. Resulting monolayers were visible under the
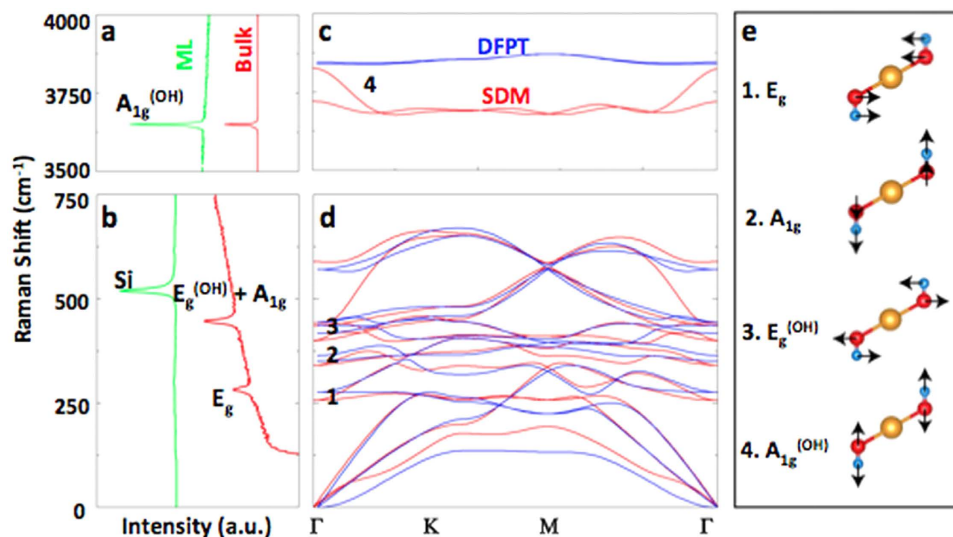
Figure 2. Phonon dispersion and Raman spectrum of $Mg(OH)_2$. Raman spectroscopy measurements taken from thick flakes and monolayers of $Mg(OH)_2$ in the (**a**) high frequency (3500–4000 cm^{-1}) and (**b**) low frequency (0–750 cm^{-1}) range. (**c-d**) Phonon dispersion calculated by density functional perturbation theory (DFPT) in blue and small displacement method (SDM) in red for high and low frequencies, respectively. (**e**) Corresponding optical modes highlighted in Fig. 2a,b.

optical microscope, but appeared faint or dull compared to MoS_2 on 90 nm SiO_2. Contact mode atomic force microscopy (AFM) measurements show that each $Mg(OH)_2$ layer is ~0.85–0.95 nm in thickness (Fig. 1d).

Even though $Mg(OH)_2$ quickly becomes unstable under e-beam irradiation due to relatively weak bonds lost by collusion with electrons, the monolayer is stable in ambient conditions as determined by AFM and Raman measurements: the surface morphology, smoothness, and Raman spectrum show no sign of surface degradation within a three-month timeframe and are superior to metastable or unstable 2D materials such as silicene[16–18], black phosphorus[19], $MoTe_2$[20], and GaTe. Prolonged environmental stability of $Mg(OH)_2$ is most likely related to strongly bonded hydrogen and oxygen atoms in –OH groups creating chemically passivated surfaces.

Lattice dynamics of $Mg(OH)_2$

The unit cell of the $Mg(OH)_2$ contains five atoms (Fig. 1a); therefore, the phonon dispersion yields three acoustic and 12 optical modes where the vibration representation of the optical modes at zone center is described as $\Gamma = 4E_u + 2A_{2u} + 4E_g + 2A_{1g}$[21]. These modes for monolayer $Mg(OH)_2$ are calculated by small displacement method (SDM) and density functional perturbation technique (DFPT), as shown in Fig. 2c,d (red and blue lines), and compared to the Raman spectrum of monolayer as well as bulk $Mg(OH)_2$ flakes in Fig. 2a,b. In the back scattering configuration, like in our spectrometer, only E_g and A_{1g} modes (Fig. 2e) can be observed experimentally. E_g and A_{1g} modes, shown in Fig. 2e, have the translational motion, meaning O-H bond distance is mostly fixed, whereas E_g^{OH} and A_{1g}^{OH} modes correspond to the librational vibration of O and H atoms where O-H bond distance changes. Modes indexed with (OH) are undefined for TMDs, e.g. MoS_2 and $MoSe_2$, as the –OH groups are replaced by chalcogens and the presence of these modes are the primary difference between $Mg(OH)_2$, or AMHs family members, and TMDs[22].

Raman spectrum of bulk $Mg(OH)_2$ displays two prominent peaks located at 280 and 445 cm^{-1} (Fig.2b red solid line), where the first peak is associated with E_g mode and the second peak is a combination of (degenerate) of A_{1g} and E_g^{OH} modes (see Figure S2). As the material is thinned to a monolayer (green solid lines), these peaks completely disappear due to the low optical absorption coefficient of wide band gap $Mg(OH)_2$. Consequently, low-frequency Raman peaks offer no substantial information on mono- and few-layers (< 10 layers), and in fact the material analysis and quantification cannot be performed by usual first order Raman modes (E_g and A_g). On the other hand, A_{1g}^{OH} is a breathing mode of the –OH group when the alkaline atom is stationary which involves O and H atom motion in the out-of-plane direction. Since both H and O atoms are light, its peak position appears at very high frequencies ($\omega \sim 3650$ cm^{-1}) as shown in Fig. 2a. Unlike E_g, A_{1g}, and E_g^{OH} modes, $A_g^{(OH)}$ peak is observed clearly from bulk to monolayers owing to its large Raman scattering cross-section under visible (488 nm) excitation.

Anomalous dimensionality effects from 3D to 2D

Presence of A_{1g}^{OH} peak for 2D $Mg(OH)_2$ is clearly seen from Raman mapping measurements on exfoliated flakes. Mapping at 3650 cm^{-1} shows that A_{1g}^{OH} peak intensity gradually decreases from thick to 2D regions due to weak Raman scattering from thinner (lesser) materials, but $A_{1g}^{OH(1)}$ signal remains finite for 2D sheets. A closer look at the A_{1g}^{OH} mode (Fig. 3c) shows that its peak shape dramatically changes, as flakes are isolated down to 2D. The doublet feature (green and blue curves) observed for bulk and thick flakes transforming into one single peak (red curve) in the 2D limit as shown at the top of Fig. 3c. In this regard, the peak shape of $A_g^{(OH)}$ provides a quick way to assess the material thickness and presence of 2D $Mg(OH)_2$.
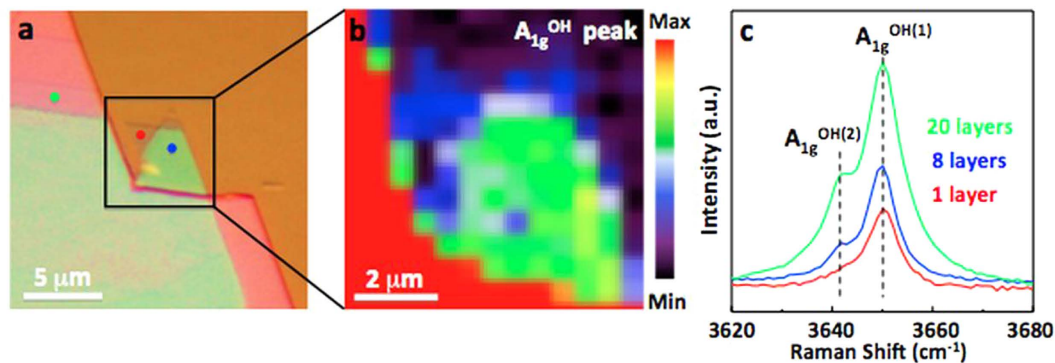
Figure 3. Anomalous Lattice Vibration in 2D $Mg(OH)_2$ (**a**) Optical image of mapped $Mg(OH)_2$ flakes. (**b**) Actual Raman mapping at 3650 cm^{-1} for A_{1g}^{OH} mode. (**c**) Representative Raman spectrum acquired from highlighted thick (green), few-layer (blue), and monolayer (red) regions (see data acquisition points in Fig. 3a).
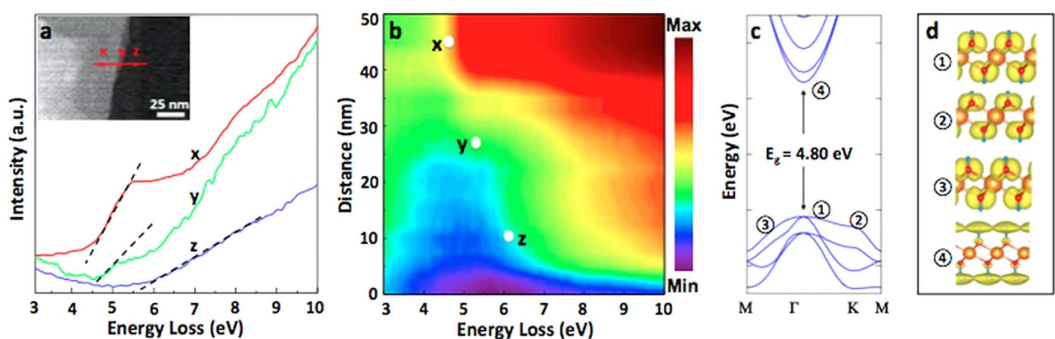
Figure 4. Nano-EELS measurements and band renormalization in 2D $Mg(OH)_2$ (**a**) Nano scale Electron Energy Loss Spectra (nano-EELS) on thick- (x), few- (y), and mono- (x) layered $Mg(OH)_2$ sheets. (**b**) Nano-EELS mapping on $Mg(OH)_2$ thick, few-, and mono- layered flakes. (**c**) Calculated electronic band structure of monolayer $Mg(OH)_2$. (**d**) Orbital characters of bands located at some of the high symmetry points highlighted in the calculated band structures.

To understand the dimensionality effects observed on $A_g^{(OH)}$ mode, we decomposed $A_g^{(OH)}$ into two peaks -located at 3650 and 3642 cm^{-1}-, and labeled them as $A_{1g}^{OH(1)}$ and $A_{1g}^{OH(2)}$ for easy reference (Fig. 3c). DFT vibrational spectrum analysis of their eigen-motions shows that these two peaks are associated with in-phase and out-of-phase –OH breathing modes between adjacent layers and estimated to be separated by 10.7 cm^{-1}. This closely aligns with the experimentally determined value of $\Delta\omega \sim 8\,cm^{-1}$. More specifically, if A_{1g}^{OH} mode (–OH bonds) in one layer is stretching (bond distance is increasing) and –OH bonds in the adjacent layers are contracting (bond length is decreasing), this mode is called the out-of-phase vibration and labeled as $A_{1g}^{OH(1)}$. In this mode, the restoring forces on –OH groups are minimized by geometrical consideration, and thus yield a softer mode at lower frequencies. Similarly, the interaction (restoring force) is greater when the OH breathing motion of all the layers are in-phase, and hence $A_{1g}^{OH(2)}$ appears at lower frequencies (by $\sim 8\,cm^{-1}$). Based on this model, after flakes are isolated to 2D, $A_{1g}^{OH(2)}$ mode becomes absolute (there is no nearby –OH group acting as a large restoring force on the monolayer), leaving a single Raman peak in the close vicinity of $A_{1g}^{OH(2)}$ mode (Fig. 3c red).

Dimensionality effects on the electronic structure of $Mg(OH)_2$

We performed nm spatial resolution and probing spot electron energy-loss spectroscopy (nano-ELLS) on mono-, few-, and thick- layered $Mg(OH)_2$ sheets deposited onto TEM grids to estimate the electronic band gap of the material for different numbers of layers (Fig. 4a). Notice that photoluminescence measurements under 325 nm laser excitation yield zero PL intensity likely due to low optical absorption as well as large non-radiative recombination; and thus, nano-EELS measurements are essential for understanding the effects of dimensionality on the electronic properties of $Mg(OH)_2$.

When incoming electron energy closely matches the electronic band gap of the material, electrons are absorbed by the material and lose some of their kinetic energies. At this energy point, the intensity of EELS spectrum sharply increases and extrapolation of this slope to the abscissa (energy) yields the band gap value of the material[23]. Figure 4a shows the EELS spectra collected from thick (point x) to monolayer (point z) segments of the $Mg(OH)_2$ flake on a TEM grid (Fig. 4a inset). It can be seen in Fig. 4a that the band gap increases from 4.6–5.5 eV going from point x to point z as a result of band renormalization, confinement effects in 2D insulating materials, and presented nano-EELS measurements mark the first experimental demonstration of band normalization in layered insulating material. Dimensionality-induced shift in the band gap value of $Mg(OH)_2$ can be
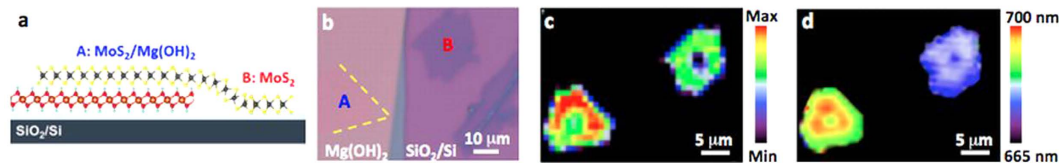
Figure 5. Heterostructure of MoS2/Mg(OH)$_2$ (**a**) Schematic presentation of demonstrated MoS$_2$/Mg(OH)$_2$ heterostructure on SiO$_2$/Si substrate. (**b**) Optical images taken from MoS$_2$/Mg(OH)$_2$ heterostructure (**A**, bule) and pristine MoS$_2$ (**B**, red) on SiO$_2$/Si substrate. (**c**) Integrated PL intensity and (**d**) PL peak position mapping at the selected area in Fig. 5b.

observed from the nano-EELS mapping depicted in Fig. 4b. Observe that these band values are suitably located between semiconducting TMDs[24,25] and insulating h-BN (6 eV or larger)[26,27], expanding the library of available 2D materials.

Theoretically, the electronic band structure of 2D Mg(OH)$_2$ along high symmetry points in the first Brillouin zone is shown in Fig. 4c. Based on DFT calculations, monolayer Mg(OH)$_2$ is a direct band gap insulator with optical gap values of 4.80 eV (theoretical) and the valance band maximum (VBM) and conduction band minimum (CBM) located at the Γ symmetry point. In Fig. 4d, we show band- and k-point decomposed charge density of band edges at fixed iso-values (isosurface-level is set to 0.0196). Orbital analysis results indicate that the first (VBM at Γ) and third points (VBM at M) involve p$_x$ and p$_y$ orbitals of O atoms, whereas the second band at (VBM at K) has p$_z$ orbital character. The fourth band (CBM at Γ) exhibits a well-delocalized state over the surface, a free-electron-like state, and the charge density which is almost not visible becomes visible with the choice of a very low iso-value.

Observed discrepancy between experimentally and theoretically estimated optical band gap values is anticipated as DFT calculations typically underestimate the band gap values due to lack of proper description of functionals used in calculations. These deficiencies are particularly apparent from DFT calculations on bulk Mg(OH)$_2$, predicting larger band gap value compared to monolayers, which conflicts with band renormalization theory within the quantum confinement limit as well as our experimentally determined values ($E_g^{Bulk} < E_g 2D$). Nevertheless, calculated band offset values have been summarized in supplementary information S1.

Surface polarization and Mg(OH)$_2$/MoS$_2$ heterostructures

DFT Bader charge transfer analysis reveals that 0.9 e$^-$/atom and 0.5 e$^-$/atom charges transfer from Mg to O atoms and H to O atoms respectively. The charge transfer between Mg, O, and H creates a highly polarized (charged) surface which is, in principle, capable of providing (transferring) extra carriers into dissimilar 2D materials, e.g. MoS$_2$ and MoSe$_2$, when in contact with Mg(OH)$_2$ layers in the vertical heterojunction geometry (Fig. 5a). We anticipate that substrate induced self-doping effect provides an efficient way to enhance PL intensity of MoS$_2$ by tuning the neutral (eh) to a charged (eeh) exciton population after withdrawing electrons from unintentionally n-doped MoS$_2$ monolayers, along with creating a more uniform charge density on the MoS$_2$ surface.

Based on this self-doping mechanism, we fabricated vertical MoS$_2$/Mg(OH)$_2$ heterojunctions by transferring CVD grown MoS$_2$ monolayers onto exfoliated few-layered Mg(OH)$_2$ flakes on SiO$_2$/Si substrates, shown as flake A in Fig. 5b. Single point PL measurements reveal that light emission intensity increases considerably after MoS$_2$ is transferred onto Mg(OH)$_2$. As shown in Fig. 5c, this PL enhancement effect and related PL peak shift can be clearly seen on the MoS$_2$/Mg(OH)$_2$ region (flake A), where integrated PL intensity increases as much as 100% with a PL peak position change from 1.83 eV (for pristine MoS$_2$) to 1.81 eV (Fig. 5d). Similar trends and PL enhancement were observed on more than 20 separately fabricated samples.

The observed changes in the PL peak intensity and peak position can be explicated by the following physical mechanisms. Previously, PL intensity of sTMDs monolayers was modulated for more than an order of magnitude by changing the sheet carrier concentration with various techniques such as inter-molecular gating[28] and conventional back-gate biasing[28,29]. We found that in close proximity to undoped (doped) limit, the light emission is strong (weak) and the emission process is mostly dominated by efficient (inefficient) neutral excitons (trions)[29]. Within this picture, after MoS$_2$ is deposited onto few-layer thick Mg(OH)$_2$, an electron is transferred from MoS$_2$ to Mg(OH)$_2$ due to presence of an excess amount of electrons on the MoS$_2$ side. These access carriers in MoS$_2$ have been previously reported and speculated to originate from chalcogen vacancies and/or unintentional impurities introduced during CVD growth, and immediately transfer to a positively charged Mg(OH)$_2$ surface. Consequently, MoS$_2$ layers are relatively depleted, forming efficient (luminescent) neutral exciton complexes and enhancing the PL intensity.

Using modified Mg(OH)$_2$ crystal growth technique, 2D insulating Mg(OH)$_2$ sheets are isolated to monolayers from their bulk counter-parts, allowing to study its vibrational and electronic properties of 2D Mg(OH)$_2$ for the first time. We find that its vibrational properties are vastly different from other 2D materials known to date. Raman spectroscopy and vibration analysis reveal that hydroxyl group out-of-plane breathing mode located at high frequencies (~3650 cm^{-1}) dominates the lattice modes, which dictates the dimensionality effects and provides an effective way to characterize 2D Mg(OH)$_2$ sheets. In addition, nano-EELS measurements allowed us to link electronic properties to the number of layers for the first time on 2D insulating materials, pointing towards unusual quantum confinement effects in Mg(OH)$_2$. Heterostructures of CVD MoS$_2$ monolayers on highly polar Mg(OH)$_2$ facilitate a large charge transfer at the Mg(OH)$_2$–MoS$_2$ interface, providing effective means to manipulate excitonic dynamics. Results not only establish unusual confinement effects in 2D Mg(OH)$_2$, but also offer

novel 2D insulating material with unique physical, vibrational, and chemical properties for potential applications in flexible optoelectronics.

Methods

CVD growth. MoS_2 monolayers were produced by CVD technique. Si with 300 nm SiO_2 was used as a growth substrate. The substrates were cleaned in piranha solution (H_2SO_4:H_2O_2;3:1) and then they were placed with face up above on to the top of alumina boat which was containing 3.5 mg MoO_3 ($\geq$99.5% Sigma Aldrich). The ceramic boat was placed to the center of the heating zone of the furnace. Another alumina crucible containing sulphur ($\geq$99.88% Sigma Aldrich) was placed in to the tube in a gas flow direction. The distance between substrates and sulphur containing boat was 23 cm. the monolayer growth was performed under atmospheric pressure with high purity nitrogen. The furnace heated to 575 °C with 140 s.c.c.m. and then flow rate was decreased to 40 s.c.c.m. After melting of the sulphur at 665 °C, flow rate was decreased to 5 s.c.c.m. and then the temperature kept at 690 °C with 5 s.c.c.m. for 10 minutes. Samples cooled down to the 500 °C at a rate of 21 °C min^{-1} with 40 s.c.c.m. When the temperature was 500 °C , the furnace opened and samples cooled down to the room temperature quickly.

Crystal growth. AMHs crystals were synthesized using hydrothermal growth routes by two different precursor reactants. The first technique was based on reaction between alkaline metal nitrates, $Mg(NO_3)_2$ Here, purified $Mg(NO_3)_2$ solution was placed in a autoclave chamber and was heated to 125 °C for 6 hours and then NH_3 was introduced into the autoclave and kept at the same temperature for 1–3 days. The reaction chamber was slowly cooled down to room temperature and the materials were separated from the reaction solution by standard filtration to be dried at 105 °C in vacuum. In the second technique $Mg(NO_3)_2$ (0.05 M) and $N_2H_4 \cdot H_2O$ was mixed to form precipitation and rest of the reaction occured in teflon lined stainless steel autoclave at 165 °C for 1–3 days. Grown materials were centrifuged, filtered, washed with distilled water, and dried in vacuum at 100 °C. Synthesized crystals were around couple Teflon-lined stainless steel autoclave lamellar behavior with transparent look. XRD measurements on the $Mg(OH)_2$ displayed sharp 0001 peak that correspond to 4.86 A interlayer spacing values which is in close agreement with the c-axis values estimated from our DFT calculations (Figure S1).

Heterostructure fabrication. The heterostructure was fabricated by transferring CVD-grown MoS_2 monolayers (described above) onto exfoliated $Mg(OH)_2$ flakes on SiO_2/Si substrate. The monolayer MoS_2 flakes were first covered by Poly(dimethyl siloxane) (PDMS, Sylgard 184, Dow Corning) film which were prepared by mixing its precursors followed by heat curing at 75 °C for 30 mins. Then, the MoS_2 single-layers were transferred onto PDMS from SiO_2/Si substrate by heated KOH (1 mol/L) etching at 60 °C The KOH residue was further removed by cleaning the detached PDMS/MoS_2 film in deionized water. After dried by nitrogen flow, the film was finally adhered onto $Mg(OH)_2$ thin flakes for 30 mins. before peeled off. Note, the MoS_2/$Mg(OH)_2$ heterostructure can be successfully prepared using the above method due to the highly polarized $Mg(OH)_2$ surface, as well as the lower surface energy of SiO_2/Si substrate

Spectroscopy and optical measurements. The photoluminescence and Raman measurements were performed in a Renishaw InVia Raman microscope by using a laser excitation source of wavelength 488 nm under 100× objective lens (0.95 NA). Laser power was set to 1 mW on 10 mm^2 area.

Nano-EELS measurements. (Valence electron energy loss spectroscopy) was performed using Nion High-Resolution Monochromated EELS STEM (HERMES) system consisting of a Nion STEM100 scanning transmission electron microscope (STEM) equipped with a Nion high energy resolution monochromator and a modified Gatan Enfinium EEL spectrometer. The energy resolution, measured from the half width of the zero-loss peak was set to be 60 meV, to improve S/N, and the accelerating voltage was 60 kV, the probe size was about 0.3 nm, and the probe current was approximately 12 pA .

Theoretical calculations. The calculations were performed using the Vienna ab initio simulation package (VASP)[30,31]. The core-valence interaction was described by the frozen-core projector augmented wave (PAW) method[32]. Both the generalized gradient approximation of Perdew-Burke-Ernzerhof (GGA-PBE)[33] and the Heyd-Scuseria-Ernzerhof (HSE06) hybrid functional[34] were adopted for exchange-correlation functional. Energy cut off for plane-wave expansion was set to 500 eV. The Brillouin zone was sampled by 12 × 12 × 1 (12 × 12 × 9 for bulk) Monkhorst-Pack (MP) special k point meshes. A vacuum layer larger than 10 Å was added to avoid interaction between adjacent images. Structure relaxation was stopped when the force on each atom was smaller than 0.01 eV/Å. For MoS2, spin-orbit interaction was taken into account when calculating band structures. The vacuum level was taken as zero reference in the calculations of band alignment. For the calculation of phonon dispersions we utilize both small displacement (SD) and density functional perturbation theory (DFPT) methodology[35,36]. While DFPT calculations performed using the primitive unitcell of metal hydroxides, in SD calculations for the convergence of dynamical matrix we use 5 × 5 × 1 supercell.

References

1. Akinwande, D., Petrone, N. & Hone, J. Two-dimensional flexible nanoelectronics. *Nat Commun.* **5,** 5678 (2014).
2. Wang, Q. H., Kalantar-Zadeh, K., Kis, A., Coleman, J. N. & Strano M. S. Electronics and optoelectronics of two-dimensional transition metal dichalcogenides. *Nat Nanotech.* **7,** 699–712 (2012).
3. Novoselov, K. S. *et al.* Two-dimensional atomic crystals. *Proc. Natl. Acad. Sci.* **102,** 10451–10453 (2005).
4. Mak, K., Lee, C., Hone, J., Shan, J. & Heinz, T. F. Atomically thin MoS_2: a new direct-gap semiconductor. *Phys. Rev. Lett.* **105,** 136805 (2010).
5. Splendiani, A. *et al.* Emerging photoluminescence in monolayer MoS_2. *Nano Lett.* **10,** 1271–1275 (2010).
6. Radisavljevic, B., Radenovic, A., Brivio, J., Giacometti, V. & Kis, A. Single-layer MoS2 transistors. *Nat. Nanotech.* **6,** 147–150 (2012).

7. Tongay, S. *et al.* Thermally driven crossover from indirect toward direct bandgap in 2D semiconductors: MoSe$_2$ versus MoS$_2$. *Nano Lett.* **12,** 5576–5580 (2012).
8. Zhao, W. *et al.* Evolution of electronic structure in atomically thin sheets of WS$_2$ and WSe$_2$. *ACS Nano* **7,** 791–797 (2013).
9. Kim, J. *et al.* Ultrafast generation of pseudo-magnetic field for valley excitons in WSe$_2$ monolayer. *Science*, **346,** 6214 (2014).
10. Mak, K. F. *et al.* Tightly bound trions in monolayer MoS$_2$. *Nat Mater.* **12,** 207–211 (2012).
11. Xu, X., Yao, W. & Heinz, T. F. Spin and pseudospins in layered transition metal dichalcogenides. *Nat Phys.* **10,** 343–350 (2014).
12. Li, Y. *et al.* Preparation of Mg(OH)$_2$ nanorods. *Adv Mat.* **12,** 818–821 (2000).
13. Lieth, R. M. A. Preparation and Crystal Growth of Materials with Layered Structures Vol. 1 (eds Lieth, R. *et al.*) Ch. 4, 141–243 (Springer, 1977).
14. Jochym P. T. *et al.* Structure and elastic properties of Mg(OH)$_2$ from density functional theory. *J Phys Condens Matter.* **22,** 445403 (2010).
15. Jin, D. *et al.* Hydrothermal synthesis and characterization of hexagonal Mg(OH)$_2$ nano-flake as a flame retardant. *Mat Chem & Phys.* **112,** 962–965 (2008).
16. Acun, A., Poelsema, B., Zandvliet, H. J. W. & Van Gastel, R., The instability of silicene on Ag (111). *App Phys Lett.* **103,** 263119 (2013).
17. Liu, G., Lei, X. L., Wu, M. S., Xu, B. & Ouyang, C. Y. Is silicene stable in O$_2$?—First-principles study of O$_2$ dissociation and O$_2$−dissociation–induced oxygen atoms adsorption on free-standing silicene. *EP.* **106,** 47001 (2014).
18. Sahin, H., Sivek, J., Li, S., Pattoens, B. & Peeters F. M. Stone-Wales defects in silicene: Formation, stability, and reactivity of defect sites. *Phys Rev* B. **88,** 45434 (2013).
19. Wood, J. D. *et al.* Effective Passivation of Exfoliated Black Phosphorus Transistors against Ambient Degradation. *Nano Lett.* **14,** 6964–6970 (2014).
20. Chen, B. *et al.* Environmental Changes in MoTe$_2$ Excitonic Dynamics by Defects-Activated Molecular Interaction. *ACS Nano* **9,** 5326–5332 (2015).
21. Dawson, P., Hadfield, C. D. & Wilkinson, G. R. The polarized infrared and Raman spectra of Mg(OH)$_2$ and Ca(OH)$_2$. *J. Phys. Chem. Sol.* **34,** 1217–1225 (1972).
22. Lee, C., Yan, H., Brus, L. E., Heinz, T. F. & Hone, J. Anomalous Lattice Vibrations of Single- and Few-Layer MoS$_2$. *ACS Nano* **4,** 2695–2700 (2010).
23. Erni, R. & Browning, N. D. Valence electron energy-loss spectroscopy in monochromated scanning transmission electron microscopy. *Ultramicroscopy* **104,** 176–192 (2005).
24. Tongay, S. *et al.* Defects activated photoluminescence in two-dimensional semiconductors: interplay between bound, charged, and free excitons. *Sci. Rep.* **3,** 2657 (2013).
25. Ataca, C., Sahin, H. & Ciraci, S. Stable, single-layer MX$_2$ transition-metal oxides and dichalcogenides in a honeycomb-like structure. *J. Phys. Chem* C **116,** 8983–8999 (2012).
26. Watanabe, K., Taniguchi, T. & Kanda, H. Direct-bandgap properties and evidence for ultraviolet lasing of hexagonal boron nitride single crystal. *Natt Mat.* **3,** 404–409 (2004).
27. Dean, C. R. *et al.* Boron nitride substrates for high-quality graphene electronics. *Nat. Nano.* **5,** 722–726 (2010).
28. Tongay, S. *et al.* "Broad-range modulation of light emission in two-dimensional semiconductors by molecular physisorption gating. *Nano Lett.* **6,** 2831–2836 (2013).
29. Newaz, A. K. M. *et al.* Electrical control of optical properties of monolayer MoS$_2$. *Solid State Commun.* **155,** 49–52 (2013).
30. Kresse, G. & Hafner, J. Ab initio molecular dynamics for liquid metals. *Phys. Rev. B* **47,** 558–561 (1993).
31. Kresse, G. & Furthmuller, J. Efficiency of ab-initio total energy calculations for metals and semiconductors using a plane-wave basis set. *Comp Mater Sci.* **6,** 15–50 (1996).
32. Blochl, P. E. Projector augmented-wave method. *Phys. Rev. B* **50,** 17953–17979 (1994).
33. Perdew John, P., Burke, K. & Ernzerhof, M. Generalized Gradient Approximation Made Simple. *Phys. Rev. Lett.* **77,** 3865 (1996).
34. Heyd, J., Scuseria, G. E. & Ernzerhof, M. Hybrid functionals based on a screened Coulomb potential. *J. Chem. Phys.* **118,** 8207 (2003).
35. Alfe, D. PHON: A program to calculate phonons using the small displacement method. *Comput. Phys. Commun.* **180,** 2622 (2009).
36. Baroni, S., Gironcoli, S., Dal Corso, A. & Giannozzi, P. Phonons and related crystal properties from density-functional perturbation theory. *Rev. Mod. Phys.* **73,** 515 (2001).

Acknowledgements

Author Contributions

All the authors have directly contributed to this work. All authors have given their approval prior to the submission and helped preparation of this manuscript. S.T. designed and managed the project. A.S. and K.W. designed and performed the measurements. H.S., J.K., S.H.S. and F.M.P. performed calculations and discussed the results. B.C. performed AFM measurements. S.Y., K.W. and H.C. prepared TEM samples and heterojunctions. T.A. and S.T. performed nano-EELS. A.S., K.W., H.S. and S.T. wrote the manuscript. The manuscript has been discussed with all the authors.

Additional Information

Supplementary information accompanies this paper at http://www.nature.com/srep

Competing financial interests: The authors declare no competing financial interests.

How to cite this article: Suslu, A. *et al.* Unusual dimensionality effects and surface charge density in 2D Mg(OH)$_2$. *Sci. Rep.* **6,** 20525; doi: 10.1038/srep20525 (2016).